Nano Research

Open Access

Research Article

Efficient and sustainable urea synthesis on a bifunctional catalyst

Di Yuan[1] ✉, Wenyu Du[2], Dongwei Ma[3], and Ke Chu[2] ✉

[1] School of Physics and Electrical Engineering, Anyang Normal University, Anyang 455000, China
[2] School of Materials Science and Engineering, Lanzhou Jiaotong University, Lanzhou 730070, China
[3] Anhui Province Industrial Generic Technology Research Center for Alumics Materials, School of Physics and Electronic Information, Huaibei Normal University, Huaibei 235000, China

Cite this article: *Nano Research*, **2025**, *18*, 94907910. https://doi.org/10.26599/NR.2025.94907910

ABSTRACT: Electrochemical co-reduction of CO_2 and nitrogen sources (N_2 or NO_3^-) provides a promising route for ambient urea synthesis, yet suffers from low conversion efficiency or reliance on fossil fuel-derived NH_3/NO_3^-. Herein, we present an integrated plasma-electrocatalytic route for sustainable urea synthesis from ambient air, which involves the initial plasma-driven air oxidation to form NO_x^- and followed by electrocatalytic co-reduction of CO_2 + NO_x^- to produce urea. Specially, a bifunctional Bi_{SA}/a-MoO_3 catalyst (isolated Bi single atom on amorphous MoO_3) was designed to promote both plasma and electrocatalytic processes, consequently achieving the exceptional urea yield rate of 55.9 $mmol \cdot h^{-1} \cdot g^{-1}$ and Faradaic efficiency of 59.7%. The combined theoretical calculations and *in situ* spectroscopic measurements reveal the synergy of Bi_{SA} and unsaturated Mo sites in boosting the C–N coupling of *COOH and *NH_2 intermediates for selective urea formation.

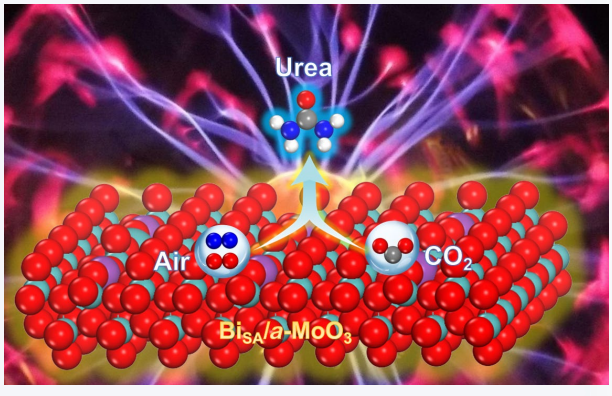

KEYWORDS: urea electrosynthesis, plasma activation, electrocatalysis, atomically dispersed catalysts

1 Introduction

Urea ($CO(NH_2)_2$), a cornerstone of global agriculture, is vital for enhancing crop productivity and maintaining food security [1]. Industrially, urea is predominantly synthesized via the Bosch–Meiser process, which combines CO_2 and NH_3 under energy-intensive conditions (150–200 °C, 150–250 bar) [2]. Such an industrial method consumes large amounts of fossil fuels to produce enormous CO_2, exacerbating significant environmental challenges.

Renewable energy-driven urea electrosynthesis using CO_2 and nitrogen resources offers a promising route to sustainable urea synthesis under ambient conditions [3]. In particular, urea electrosynthesis using N_2 and CO_2 as feedstocks receives extensive attention [4–6], whereas its practical application is hampered by the inert N≡N triple bond (941 $kJ \cdot mol^{-1}$) and poor N_2 solubility, severely limiting conversion efficiency [7]. Alternatively, NO_3^- presents distinct advantages of lower N=O bond dissociation energy (204 $kJ \cdot mol^{-1}$) and higher aqueous solubility [8–11], enabling more efficient co-reduction with CO_2 for urea synthesis [12–17]. Nevertheless, a key bottleneck of using NO_3^- feedstock still remains, as NO_3^- generation relies on the fossil-fueled Ostwald process, which generates significant carbon emissions [18]. This dependency on carbon-intensive NO_3^- feedstock weakens the decarbonization potential of urea electrosynthesis and highlights the need for more sustainable nitrogen sources.

Non-thermal plasma technology provides a breakthrough strategy, as it can efficiently cleave the inert N≡N bond of N_2 in the ambient air to generate active NO_x [19–21]. The generated NO_x can be favorably absorbed in an alkaline solution and converted predominantly into NO_2^- [20]. As a major product of plasma-driven air oxidation, NO_2^- offers a key advantage as the nitrogen feedstock for urea electrosynthesis, as the NO_3^--driven route is a 16-electron process while NO_2^- enables a more efficient 12-electron co-reduction with CO_2 to produce urea [22]. Accordingly, the NO_2^--driven pathway can effectively reduce kinetic barriers and minimize the competitive side reactions to improve the urea Faradaic efficiency (urea-FE) and yield rate (urea-YR). In addition, this plasma-electrocatalytic process replaces the fossil-fuel-derived NH_3/NO_3^- with air-derived NO_2^-, thereby establishing a truly sustainable route to urea synthesis which minimizes indirect carbon

Received: April 30, 2025; **Revised:** August 6, 2025
Accepted: August 12, 2025

✉Address correspondence to Di Yuan, yuandi@aynu.edu.cn; Ke Chu, chuk630@mail.lzjtu.cn

emissions while harnessing ambient air as an infinite and green nitrogen source.

In this work, we present an integrated plasma-electrocatalytic route to sustainable urea synthesis from ambient air, which involves the initial plasma-driven air oxidation to form NO_x^- and followed by co-electrolysis of CO_2 and plasma-derived NO_x^- to produce urea (ECNU) (Fig. 1(a)). A bifunctional $Bi_{SA}/a\text{-}MoO_3$ catalyst comprising isolated p-block Bi single atoms on amorphous MoO_3 (a-MoO_3) was designed to enhance both plasma-driven air oxidation and ECNU, exhibiting the excellent urea-YR of 55.9 $mmol \cdot h^{-1} \cdot g^{-1}$ and urea-FE of 59.7% in flow cell. The ECNU-catalyzed mechanism on $Bi_{SA}/a\text{-}MoO_3$ was systematically investigated by combining theoretical calculations with *in situ* spectroscopic measurements.

2 Results and discussion

As shown in Fig. 1(a), the plasma-electrocatalytic process first employs a non-thermal plasma discharge reactor (Fig. S1 in the Electronic Supplementary Material (ESM)) to dissociate N_2 and O_2 from air into N/O radicals, which recombine to generate the reactive NO_x. During the discharge, a bright electric spark appears inside the reactor tube (Fig. 1(b)). After 10 min discharge, the initial colorless gas stream turns reddish-brown (Fig. 1(c)), confirming NO_x formation. The plasma-derived NO_x is then bubbled into an alkaline KOH solution, where NO_x is absorbed and converted into NO_x^-. From Fig. S2 in the ESM, the control tests (no plasma discharge or Ar gas) show the negligible NO_x^- detection, indicating that the synergy of plasma and air is essential for NO_x^- production. The NO_2^- and NO_3^- concentrations are then quantitatively detected

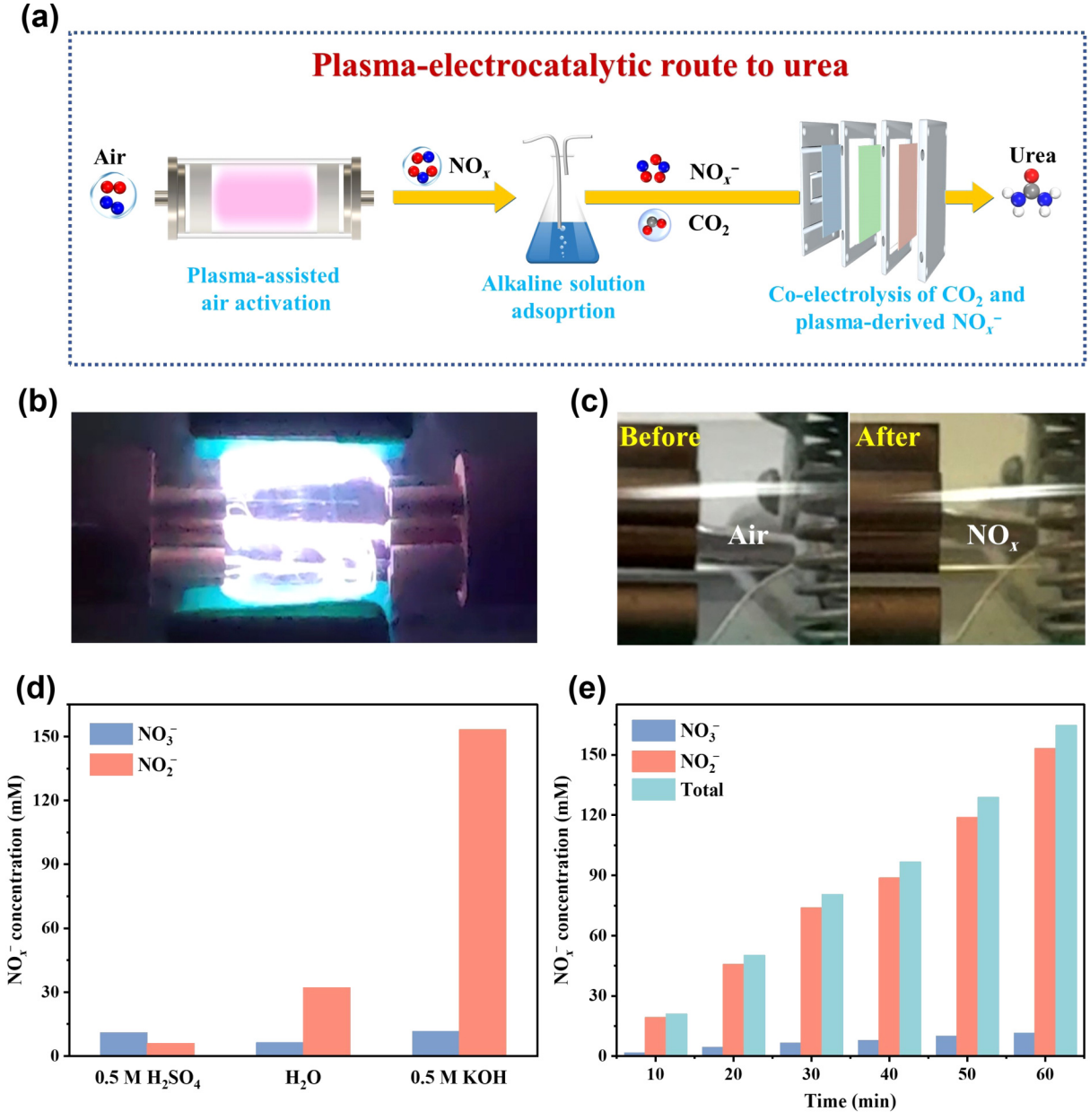

Figure 1 (a) Schematic of plasma-electrocatalytic process for urea synthesis. (b) Photograph of the tube during the plasma discharge. (c) Photographs of gas color change in the tube before and after plasma discharge for 10 min. (d) NO_x^- concentrations in different solutions after plasma discharge for 1 h. (e) NO_x^- concentrations at varying discharge times.

by the ultraviolet–visible (UV–vis) absorption spectroscopy (Figs. S3 and S4 in the ESM).

Air flow rate is an important parameter that affects gas residence time and energy conversion efficiency. As the air flow rate progressively increases, the NO_x^- concentration also rises and reaches the maximum at 23 L·min^{-1} (Fig. S5 in the ESM). In addition, as compared to acidic or neutral solutions, NO_x is more likely absorbed in alkaline solution (0.5 M KOH, Fig. 1(d)) and then converted to NO_x^- with the highest yield rate, suggesting that alkaline solution facilitates the generation of NO_x^-. After 60 min of plasma discharge at the optimal gas flow rate (23 L·min^{-1}) and in 0.5 M KOH solution, the NO_x^- concentration reaches the maximum of 153.2 mM with a corresponding NO_2^- selectivity of 93.1% (Fig. 1(e)). Moreover, after five successive cycles (Fig. S6 in the ESM), the produced NO_x^- remains above 150 mM and NO_2^- selectivity shows minor fluctuations, indicating the excellent system stability. All these findings corroborate that our plasma process enables efficient and stable NO_x^- generation, delivering a sustainable nitrogen feedstock for the downstream ECNU-driven urea electrosynthesis. Specially, the plasma-derived NO_x^- production rate is substantially increased by 35% after using Bi_{SA}/*a*-MoO_3 catalyst assembled in the plasma tube (Fig. S7(a) in the ESM), which is attributed to the enhanced activation and coupling of N_2/O_2 species on Mo/Bi_{SA} sites (Fig. S7(b) in the ESM).

Bi_{SA}/*a*-MoO_3 catalyst was prepared by a supercritical CO_2 method [23]. The X-ray diffraction (XRD) patterns of *a*-MoO_3 and Bi_{SA}/*a*-MoO_3 are shown in Fig. S8 in the ESM. It is observed that no sharp diffraction peaks are detected for both samples, confirming the amorphous structure of *a*-MoO_3. The transmission electron microscopy (TEM) image (Fig. 2(a)) shows that Bi_{SA}/*a*-MoO_3 exhibits a typical nanobelt structure. The high-resolution TEM (HRTEM) image (Fig. S9 in the ESM) reveals a disordered lattice with no apparent crystalline facets, consistent with the amorphous structure of XRD patterns (Fig. S8 in the ESM). The aberration-corrected scanning TEM (AC-STEM) image (Fig. 2(b)) clearly displays a large number of bright spots, corresponding to Bi single atoms, which are uniformly distributed on *a*-MoO_3 substrate. The corresponding atom intensity analysis and three-dimensional (3D)

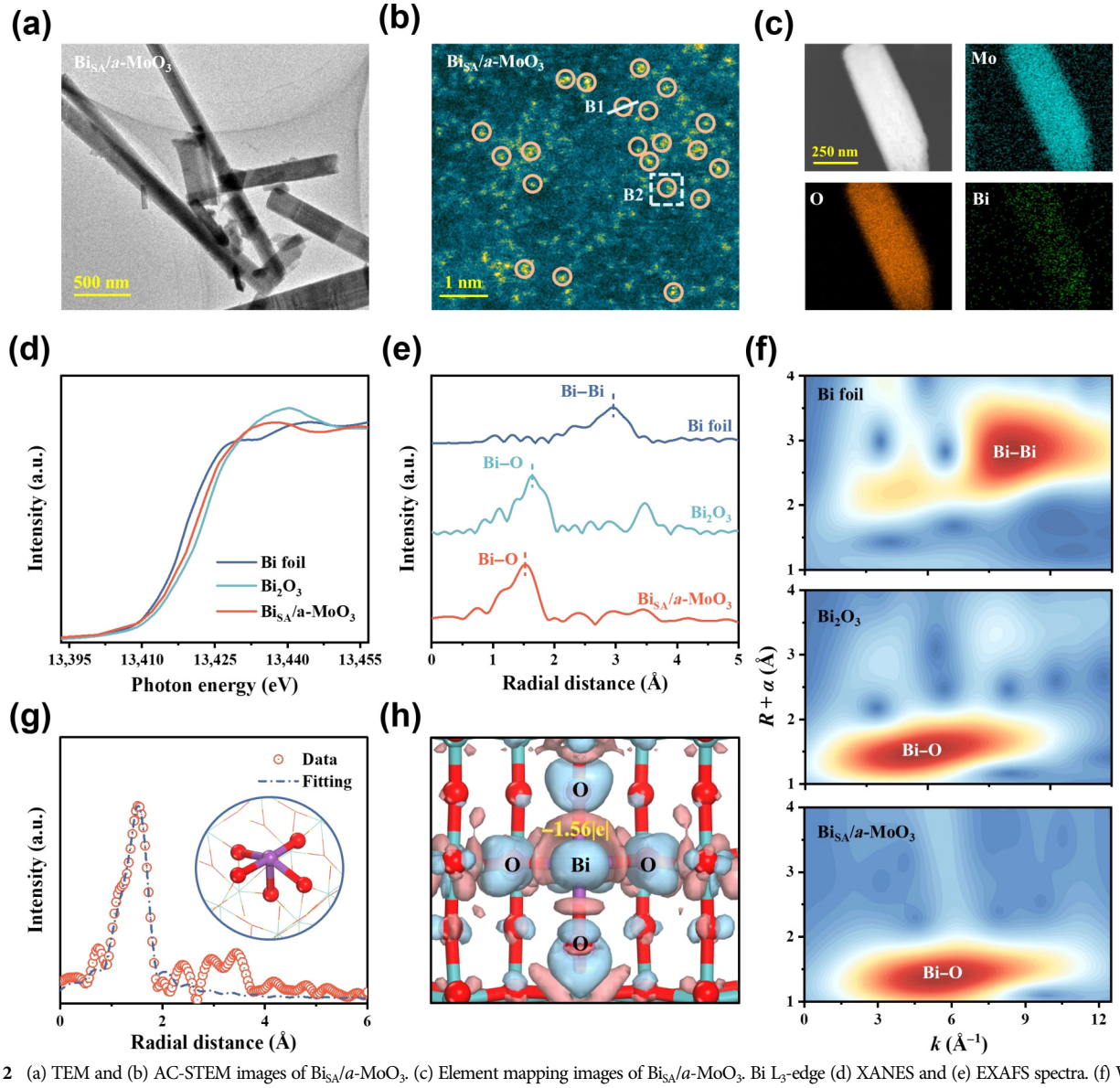

Figure 2 (a) TEM and (b) AC-STEM images of Bi_{SA}/*a*-MoO_3. (c) Element mapping images of Bi_{SA}/*a*-MoO_3. Bi L_3-edge (d) XANES and (e) EXAFS spectra. (f) Wavelet transform analyses of different samples. (g) EXAFS fitting curves of Bi_{SA}/*a*-MoO_3. (h) Charge density difference of Bi_{SA}/*a*-MoO_3.

surface plot (Fig. S10 in the ESM) reconfirm the isolation of Bi atoms [24]. In addition, the uniform distribution of Bi atoms on *a*-MoO_3 can also be seen from the elemental mapping images (Fig. 2(c)). In the electron paramagnetic resonance (EPR) spectra (Fig. S11 in the ESM), strong and similar g signals appear on *a*-MoO_3 and Bi_{SA}/*a*-MoO_3 as compared to bulk MoO_3, indicating the presence of abundant oxygen vacancies (O_v) on both catalysts.

X-ray absorption near edge structure (XANES) spectra (Fig. 2(d)) of the Bi L_3-edge were recorded to elucidate the Bi valence state in Bi_{SA}/*a*-MoO_3. The white line intensity of Bi_{SA}/*a*-MoO_3 is between that of Bi^0 in Bi foil and Bi^{3+} in Bi_2O_3, which indicates that Bi carries a partial positive charge. The extended X-ray absorption fine structure (EXAFS) analysis (Fig. 2(e)) reveals the coordination environment of Bi. The major peak at 1.53 Å corresponds to Bi–O coordination bond while no Bi–Bi bond (2.96 Å) is observed, suggesting an atomic-level dispersion of Bi with no formation of metal clusters or alloy phases [25–28]. The wavelet transform (WT) analysis (Fig. 2(f)) shows that, unlike the typical Bi–Bi intensity maximum (8.41 $Å^{-1}$) for Bi foil, there is a sole Bi–O intensity maximum at 5.46 $Å^{-1}$ for Bi_{SA}/*a*-MoO_3, confirming again that Bi exists as a single atom in Bi_{SA}/*a*-MoO_3. Moreover, a quantitative EXAFS fitting (Fig. 2(g) and Table S1 in the ESM) shows that the isolated Bi atom is coordinated with five O atoms to form a Bi_1–O_5 structure.

Density functional theory (DFT) calculations reveal the electronic interactions between isolated Bi atoms and *a*-MoO_3 substrate in Bi_{SA}/*a*-MoO_3. Charge density difference analysis (Fig. 2(h)) shows that there is a charge transfer of −1.56|e| from Bi to the neighboring O atoms. This charge redistribution can stabilize the reaction intermediates in the catalytic process [29–31]. In addition, the calculated work functions (Fig. S12 in the ESM) reveal that the addition of Bi reduces the work function of Bi_{SA}/*a*-MoO_3 (5.972 eV) compared with *a*-MoO_3 (7.480 eV). The reduction of work function facilitates the transfer of electrons between catalysts and adsorbed species, thereby facilitating the decreased activation barrier for C–N coupling [32–35].

The ECNU performance of Bi_{SA}/*a*-MoO_3 was evaluated in a flow cell (Fig. 3(a)), which can overcome the inherent limitations of CO_2 solubility and interfacial mass transfer in a traditional H-cell [36]. The electrochemical tests were performed in a CO_2-saturated

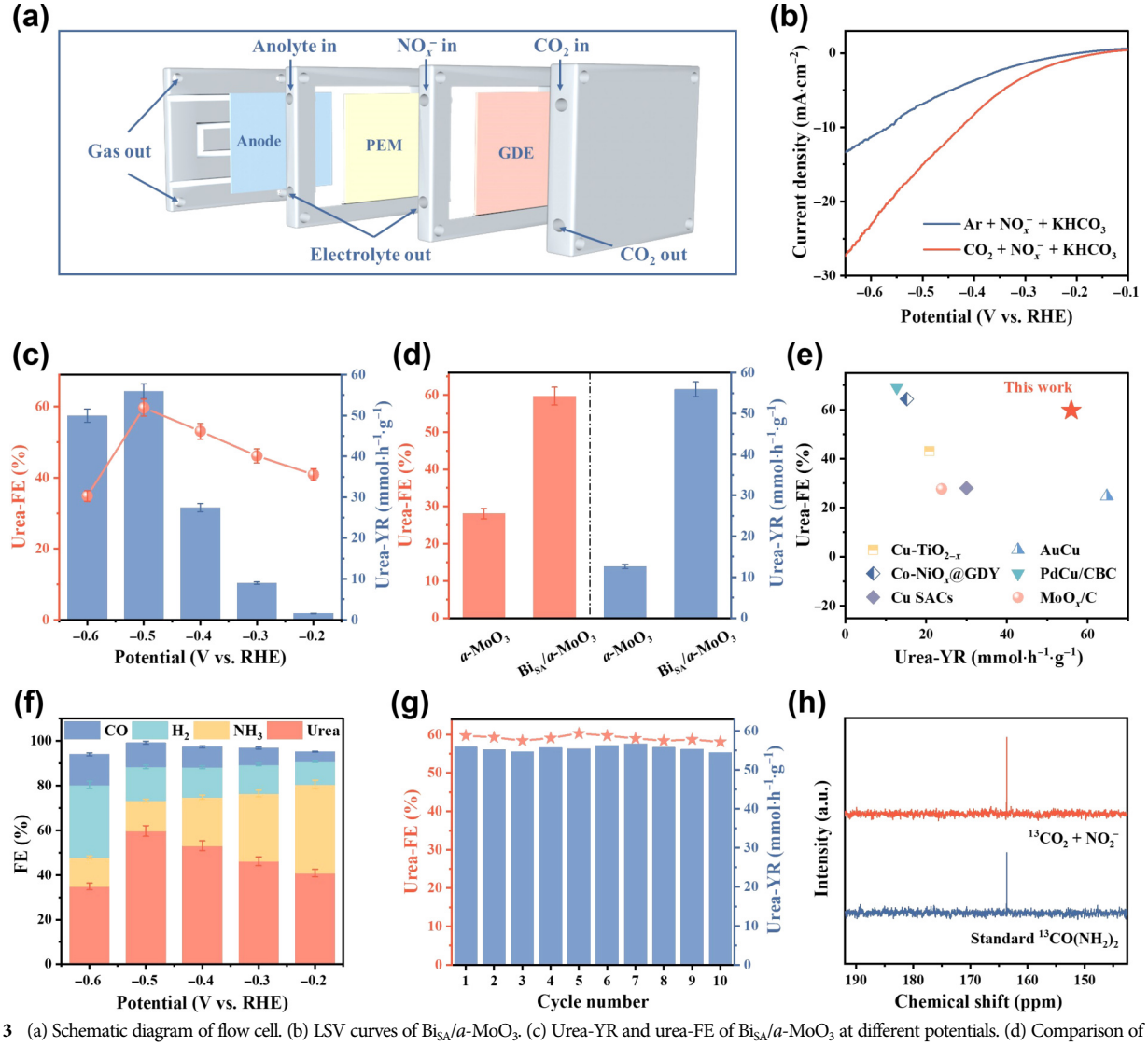

Figure 3 (a) Schematic diagram of flow cell. (b) LSV curves of Bi_{SA}/*a*-MoO_3. (c) Urea-YR and urea-FE of Bi_{SA}/*a*-MoO_3 at different potentials. (d) Comparison of ECNU performances between *a*-MoO_3, Bi_{SA}/*a*-MoO_3 and (e) reported catalysts. (f) FEs of various by-products. (g) Cycling measurement of Bi_{SA}/*a*-MoO_3 at −0.5 V. (h) ^{13}C NMR spectra using $^{13}CO_2$ as feeding gas.

aqueous electrolyte containing plasma-derived NO_x^- (diluted to 0.1 M) and 0.1 M $KHCO_3$. The electrocatalytic activity of Bi_{SA}/*a*-MoO_3 for ECNU in different gas environments was evaluated using linear scanning voltammetry (LSV). As shown in Fig. 3(b), the current density of Bi_{SA}/*a*-MoO_3 in CO_2-saturated electrolyte increases dramatically compared with that in Ar-saturated electrolyte, which indicates that Bi_{SA}/*a*-MoO_3 is catalytically active for the ECNU. To quantify the urea yield of Bi_{SA}/*a*-MoO_3-catalyzed ECNU process, chronoamperometric measurements were performed (Fig. S13 in the ESM) and the urea concentration was analyzed by UV–vis absorption spectroscopy. By-products were monitored simultaneously by both colorimetric and gas chromatographic methods (Fig. S14 in the ESM). From Fig. 3(c), the urea-FE of Bi_{SA}/*a*-MoO_3 reaches a remarkable 59.7% and the corresponding urea-YR is 55.9 $mmol \cdot h^{-1} \cdot g^{-1}$ at the optimal potential of −0.5 V. In contrast, the performance of *a*-MoO_3 under the same conditions is obviously lower (Fig. 3(d)), thus highlighting the crucial role of Bi_{SA} in substantially improving the ECNU performance. Notably, the ECNU performance of Bi_{SA}/*a*-MoO_3 is superior to the majority of reported catalysts (Fig. 3(e) and Table S2 in the ESM).

The selectivity of Bi_{SA}/*a*-MoO_3 for ECNU was evaluated by analyzing the FEs of by-products, including H_2, NH_3, and CO. As shown in Fig. 3(f), the urea-FE of Bi_{SA}/*a*-MoO_3 surpasses that of all by-products, indicating that Bi_{SA}/*a*-MoO_3 can effectively inhibit the competing side reactions while promoting the C–N coupling for urea synthesis. To verify the electrocatalytic stability of Bi_{SA}/*a*-MoO_3, 10-cycle continuous electrolysis and long-time stability tests were performed. From Fig. 3(g), the fluctuations of urea-FE and urea-YR during 10-cycle electrolysis are minimal. In addition, the current density remains stable during 100 h of continuous electrolysis (Fig. S15 in the ESM), which confirms the excellent stability of Bi_{SA}/*a*-MoO_3 in the ECNU process. During and after stability tests, Bi_{SA}/*a*-MoO_3 maintains its original structural states for both Bi_{SA} (Fig. S16 in the ESM) and *a*-MoO_3 (Fig. S17 in the ESM), confirming the robust catalyst structure.

The nuclear magnetic resonance (NMR) experiments using $^{13}CO_2$ and $K^{15}NO_2$ as feedstocks were carried out to clarify C and N sources in the ECNU electrolysis. It is shown in Fig. 3(h) that the ^{13}C NMR spectra reveal obvious resonance peaks which are consistent with the chemical shifts of ^{13}C-labeled urea, proving that CO_2 is the only C source [37]. Meanwhile, ^1H NMR analysis (Fig. S18 in the ESM) with $K^{15}NO_2$ as the electrolyte shows the characteristic peaks identical to the standard $CO(^{15}NH_2)_2$ spectra, which identifies NO_x^- as the only N precursor [37]. Moreover, the energy consumption calculations (Fig. S19 in the ESM) show that our plasma-electrocatalytic route (~ 37.4 $kWh \cdot kg^{-1}$ urea) is less energy efficient than the mature Bosch–Meiser process (~ 11.7 $kWh \cdot kg^{-1}$ urea) [38]. Nevertheless, our plasma-electrocatalytic process operates at ambient conditions and avoids fossil-derived NH_3/NO_3^-. Future work will focus on the optimization of ECNU catalyst and plasma reactor scaling to close this energy consumption gap while leveraging renewable electricity.

The catalytic mechanism of Bi_{SA}/*a*-MoO_3 was analyzed by the combined DFT calculations and *in situ* spectroscopic measurements. Since NO_2^- accounts for 93.1% of the plasma-derived NO_x^- solution (Fig. 1(d)), the theoretical ECNU analysis focuses on the NO_2^-/CO_2 co-electrolysis process. In addition, Bi_{SA} site and O_v-induced unsaturated Mo (u-Mo) site serve as the potential active sites for catalyzing the ECNU. As the adsorption of NO_2^- and CO_2 on catalyst surface is crucial for triggering the ECNU, we firstly investigated the NO_2^-/CO_2 adsorption behaviors on both Bi_{SA} site and u-Mo site of Bi_{SA}/*a*-MoO_3. It is seen from Fig. 4(a) that Bi_{SA} site exhibits a more negative CO_2 adsorption energy over u-Mo site, whereas a reverse trend is observed for NO_2^- adsorption, suggesting that Bi_{SA} site tends to adsorb CO_2 while u-Mo site prefers to adsorb NO_2^-. Hence, in Bi_{SA}/*a*-MoO_3-catalyzed ECNU process, Bi_{SA} site and u-Mo site serve as the active sites for activating CO_2 and NO_2^-, respectively.

During the ECNU process, it is generally categorized into three steps of $NO_2^- \rightarrow *NH_2$, $CO_2 \rightarrow *COOH$ (*CO) as well as C–N coupling of $*NH_2$ with *COOH (*CO) → urea [37, 39, 40]. Accordingly, we firstly investigated the free energy diagrams of $NO_2^- \rightarrow *NH_2$ reduction on u-Mo sites for both Bi_{SA}/*a*-MoO_3 and bare *a*-MoO_3 catalysts (Fig. 4(b) and Figs. S20 and S21 in the ESM). It can be seen that there is a similar tendency for both catalysts with a rate-determining step (RDS) of $*NO_2 \rightarrow *NO_2H$. However, a lower RDS energy barrier is found on Bi_{SA}/*a*-MoO_3 (0.36 eV) compared to *a*-MoO_3 (0.58 eV), suggesting that $NO_2^- \rightarrow *NH_2$ is energetically more favorable to take place on Bi_{SA}/*a*-MoO_3. For $CO_2 \rightarrow *COOH$ (*CO) process, it is seen in Fig. 4(c) (Figs. S22 and S23 in the ESM) that both Bi_{SA}/*a*-MoO_3 and bare *a*-MoO_3 facilitate *COOH formation while retarding further *COOH reduction to *CO. Likewise, Bi_{SA}/*a*-MoO_3 (Bi_{SA} site) shows a much larger downhill energy change (0.88 eV) of $CO_2 \rightarrow *COOH$ compared to 0.36 eV for a-MoO_3 (u-Mo site). These findings demonstrate that Bi_{SA} not only facilitates $CO_2 \rightarrow *COOH$, it also stimulates the adjacent u-Mo site to boost $NO_2^- \rightarrow *NH_2$, thereby delivering an overall enhancement in NO_2^-/CO_2 co-activation to $*COOH/*NH_2$ on Bi_{SA}/*a*-MoO_3.

After $*COOH/*NH_2$ formation on Bi_{SA}/u-Mo sites, we further investigated the C–N coupling process of $*COOH/*NH_2$ for urea formation. Before $*COOH/*NH_2$ coupling, *COOH or $*NH_2$ are required to migrate close to each other (Fig. S24 in the ESM). Figures 4(d) and 4(e) show that the transition state (TS) energy barrier (0.65 eV) for *COOH migration from Bi_{SA} site to u-Mo site is much higher than that for $*NH_2$ migration from u-Mo site to Bi_{SA} site (0.37 eV), suggesting that the migration of $*NH_2$ is energetically more favorable and thus the $*COOH/*NH_2$ coupling primarily occurs on Bi_{SA} site. An additional free energy analysis was performed for C–N coupling of $*COOH/*NH_2$ towards urea generation (Fig. 4(f) and Fig. S25 in the ESM). It can be seen that Bi_{SA}/*a*-MoO_3 exhibits a much lower energy barrier of 0.38 eV for C–N coupling reaction ($*COOH + *NH_2 \rightarrow *COOHNH_2$) than *a*-$MoO_3$ (0.79 eV), confirming the much enhanced ECNU energetics on Bi_{SA}/*a*-MoO_3 towards the urea formation. These results reveal the synergy of Bi_{SA} and u-Mo sites on Bi_{SA}/*a*-MoO_3 in promoting the C–N coupling of critical *COOH and $*NH_2$ intermediates for target urea formation.

Figure 4(g) shows *in situ* Fourier transform infrared (FTIR) spectra on Bi_{SA}/*a*-MoO_3 from open circuit potential (OCP) to −0.6 V (Fig. S26 in the ESM). The infrared signal belonging to *COOH is monitored at 1350 cm^{-1} [39], while the infrared signals at 1660 cm^{-1} correspond to $*COOHNH_2$ intermediate [41]. In addition, the infrared bands assigned to $-NH_2$ in urea appear at 1240 and 1180 cm^{-1} [42], and the C–N coupling bond is found at 1420 cm^{-1} [42, 43]. The formation of $*NH_2$, *COOH, and $*COOHNH_2$ can be further verified by the online differential electrochemical mass spectrometry (DEMS) analysis (Fig. S27 in the ESM). These collected *in situ* FTIR and online DEMS findings are consistent with the above DFT results, demonstrating that

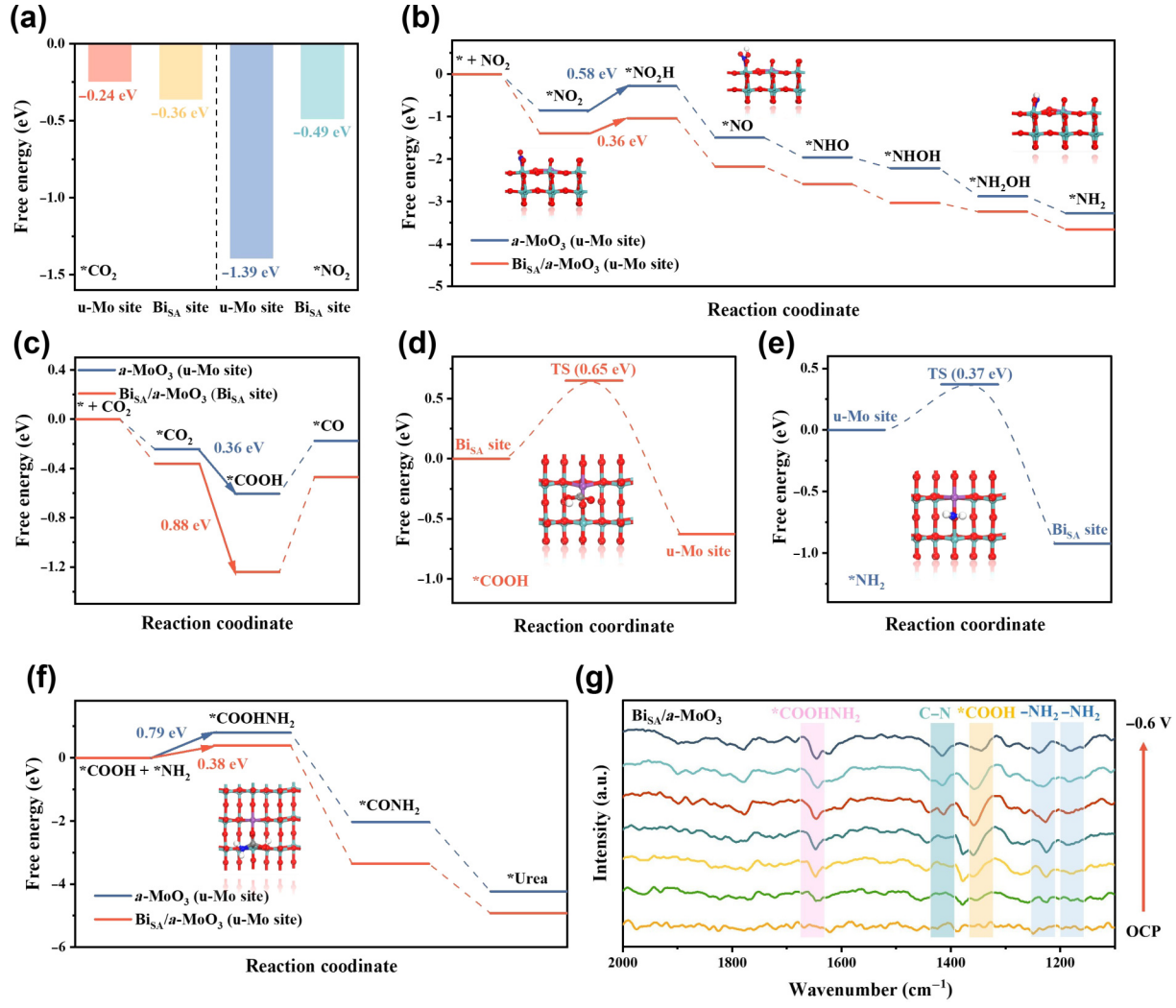

Figure 4 (a) Calculated adsorption energies of $*CO_2$ and $*NO_2$ on u-Mo site and Bi_{SA} site of Bi_{SA}/a-MoO_3. (b) Free energy maps of NO_2^- → $*NH_2$ pathway on u-Mo sites of a-MoO_3 and Bi_{SA}/a-MoO_3. (c) Free energy maps of $*CO_2$ → *CO pathway on a-MoO_3 and Bi_{SA}/a-MoO_3. ((d) and (e)) Calculated TS energy barriers for the migration of (d) *COOH from Bi_{SA} site to u-Mo site and (e) $*NH_2$ from u-Mo site to Bi_{SA} site. (f) Free energy maps of the C–N coupling process for urea generation (*COOH + $*NH_2$ → urea). (g) *In situ* FTIR spectra of Bi_{SA}/a-MoO_3 during the ECNU electrolysis from OCP to −0.6 V.

Bi_{SA}/a-MoO_3 can efficiently promote the generation of key *COOH and $*NH_2$ intermediates and their C–N coupling towards the formation of $*COOHNH_2$, which is finally converted into urea.

To investigate the selectivity of Bi_{SA}/a-MoO_3 for urea synthesis, the calculations show that $*NH_2$ intermediate on Bi_{SA}/a-MoO_3 preferentially couples with *COOH to generate $*COOHNH_2$ rather than undergoes further hydrogenation to form $*NH_3$ (Fig. S28 in the ESM). In addition, the molecular dynamics (MD, Fig. S29 in the ESM) simulations elucidate that Bi_{SA}/a-MoO_3 can inhibit the hydrogen evolution reaction (HER) effectively. The radial distribution function (RDF) analysis (Fig. S30 in the ESM) indicates that the interaction between Bi_{SA}/a-MoO_3 and NO_2^-/CO_2 species is stronger than the interaction between Bi_{SA}/a-MoO_3 and H species. These results demonstrate that Bi_{SA}/a-MoO_3 can well suppress NH_3 generation and HER, eventually enhancing the ECNU selectivity for urea synthesis.

3 Conclusions

In conclusion, the plasma-electrocatalytic approach was successfully developed to realize a truly sustainable urea synthesis from air as nitrogen resource, exhibiting high NO_x^- production rate (153.2 $mM \cdot h^{-1}$ and 93.1% NO_2^- selectivity) and excellent urea synthesis performance (urea-YR: 55.9 $mmol \cdot h^{-1} \cdot g^{-1}$ and urea-FE: 59.7%) using a bifunctional Bi_{SA}/a-MoO_3 catalyst. Mechanistic investigations unveil the synergistic effect of Bi_{SA} and u-Mo sites on promoting the C–N coupling of *COOH and $*NH_2$ intermediates for selective urea formation, while inhibiting the competitive NH_3 generation and HER. By replacing fossil-fuel-derived NH_3/NO_3^- with air-derived NO_x^-, our plasma-electrocatalytic approach paves the way for scalable and green fertilizer production and decarbonization of the chemical industry.

Electronic Supplementary Material: Supplementary material (experimental and calculation details, additional electrochemical measurements, and additional theoretical results) is available in the online version of this article at https://doi.org/10.26599/NR.2025.94907910.

Data availability

All data needed to support the conclusions in the paper are presented in the manuscript and the Electronic Supplementary

Material. Additional data related to this paper may be requested from the corresponding author upon request.

Acknowledgements

This work is supported by the Natural Science Foundation of Henan Province of China (No. 252300420313) and the Excellent Scientific Research and Innovation Team of Education Department of Anhui Province (No. 2024AH010027).

Declaration of competing interest

All the contributing authors report no conflict of interests in this work.

Author contribution statement

D. Y. performed the primary investigations, data collection/analysis, wrote the original manuscript and supervised the project. W. Y. D. performed the catalyst synthesis and characterizations. D. W. M. completed the theoretical simulations. K. C. supervised the project and provided critical input in revising and editing the manuscript. All the authors have approved the final manuscript.

Use of AI statement

None.

References

[1] Mao, C. L.; Byun, J.; MacLeod, H. W.; Maravelias, C. T.; Ozin, G. A. Green urea production for sustainable agriculture. *Joule* **2024**, *8*, 1224–1238.

[2] Kohlhaas, Y.; Tschauder, Y. S.; Plischka, W.; Simon, U.; Eichel, R. A.; Wessling, M.; Keller, R. Electrochemical urea synthesis. *Joule* **2024**, *8*, 1579–1600.

[3] Peng, X. Y.; Zeng, L. B.; Wang, D. S.; Liu, Z. B.; Li, Y.; Li, Z. J.; Yang, B.; Lei, L. C.; Dai, L. M.; Hou, Y. Electrochemical C–N coupling of CO_2 and nitrogenous small molecules for the electrosynthesis of organonitrogen compounds. *Chem. Soc. Rev.* **2023**, *52*, 2193–2237.

[4] Chen, C.; Zhu, X. R.; Wen, X. J.; Zhou, Y. Y.; Zhou, L.; Li, H.; Tao, L.; Li, Q. L.; Du, S. Q.; Liu, T. T. et al. Coupling N_2 and CO_2 in H_2O to synthesize urea under ambient conditions. *Nat. Chem.* **2020**, *12*, 717–724.

[5] Yuan, M. L.; Chen, J. W.; Zhang, H. H.; Li, Q. G.; Zhou, L.; Yang, C.; Liu, R. J.; Liu, Z. J.; Zhang, S. J.; Zhang, G. J. Host–guest molecular interaction promoted urea electrosynthesis over a precisely designed conductive metal–organic framework. *Energy Environ. Sci.* **2022**, *15*, 2084–2095.

[6] Pan, L.; Wang, J. N.; Lu, F.; Liu, Q.; Gao, Y. H.; Wang, Y.; Jiang, J. Z.; Sun, C.; Wang, J.; Wang, X. Single-atom or dual-atom in TiO_2 nanosheet: Which is the better choice for electrocatalytic urea synthesis. *Angew. Chem., Int. Ed.* **2023**, *62*, e202216835.

[7] Muhyuddin, M.; Zuccante, G.; Mustarelli, P.; Filippi, J.; Lavacchi, A.; Elbaz, L.; Chen, Y. H.; Atanassov, P.; Santoro, C. Electrochemical urea production using carbon dioxide and nitrate: State of the art and perspectives. *Energy Environ. Sci.* **2024**, *17*, 3739–3752.

[8] Wang, Y. T.; Wang, C. H.; Li, M. Y.; Yu, Y. F.; Zhang, B. Nitrate electroreduction: Mechanism insight, *in situ* characterization, performance evaluation, and challenges. *Chem. Soc. Rev.* **2021**, *50*, 6720–6733.

[9] Xu, H.; Ma, Y. Y.; Chen, J.; Zhang, W. X.; Yang, J. P. Electrocatalytic reduction of nitrate—A step towards a sustainable nitrogen cycle. *Chem. Soc. Rev.* **2022**, *51*, 2710–2758.

[10] van Langevelde, P. H.; Katsounaros, I.; Koper, M. T. M. Electrocatalytic nitrate reduction for sustainable ammonia production. *Joule* **2021**, *5*, 290–294.

[11] Zhang, Y. N.; Li, S.; Zheng, W.; Wang, X. Computational design of catalysts for ammonia synthesis. *Nano Res. Energy* **2023**, *2*, e9120068.

[12] Zhao, C.; Jin, Y.; Yuan, J. K.; Hou, Q. L.; Li, H.; Yan, X. Q.; Ou, H. H.; Yang, G. D. Tailoring activation intermediates of CO_2 initiates C–N coupling for highly selective urea electrosynthesis. *J. Am. Chem. Soc.* **2025**, *147*, 8871–8880.

[13] Ma, X. Y.; Mao, B. G.; Yu, Z. Q.; Wang, D.; Xia, J.; Hou, J. H.; Meng, X. M.; Lin, H. S. T.; Hu, C. G. Elucidating relay catalysis on copper clusters with satellite single atoms for enhanced urea electrosynthesis. *Angew. Chem., Int. Ed.* **2025**, *64*, e202423706.

[14] Chen, X. K.; Tan, Y.; Yuan, J.; Zhai, S. L.; Su, L.; Mou, Y. J.; Deng, W. Q.; Wu, H. Enhancing urea electrosynthesis from CO_2 and nitrate through high-entropy alloying. *Adv. Energy Mater.* **2025**, *15*, 2500872.

[15] Zhang, S. B.; Jin, M.; Xu, H.; Zhang, X. Y.; Shi, T. F.; Ye, Y. X.; Lin, Y.; Zheng, L. R.; Wang, G. Z.; Zhang, Y. X. et al. An oxygen-coordinated cobalt single-atom electrocatalyst boosting urea and urea peroxide production. *Energy Environ. Sci.* **2024**, *17*, 1950–1960.

[16] Li, Y.; Zheng, S. S.; Liu, H.; Xiong, Q.; Yi, H. C.; Yang, H. B.; Mei, Z. W.; Zhao, Q. H.; Yin, Z. W.; Huang, M. et al. Sequential co-reduction of nitrate and carbon dioxide enables selective urea electrosynthesis. *Nat. Commun.* **2024**, *15*, 176.

[17] Huang, D. S.; Qiu, X. F.; Huang, J. R.; Mao, M.; Liu, L. M.; Han, Y.; Zhao, Z. H.; Liao, P. Q.; Chen, X. M. Electrosynthesis of urea by using Fe_2O_3 nanoparticles encapsulated in a conductive metal–organic framework. *Nat. Synth.* **2024**, *3*, 1404–1413.

[18] Xiong, H. C.; Yu, P. P.; Chen, K. D.; Lu, S. K.; Hu, Q. K.; Cheng, T.; Xu, B. J.; Lu, Q. Urea synthesis via electrocatalytic oxidative coupling of CO with NH_3 on Pt. *Nat. Catal.* **2024**, *7*, 785–795.

[19] Li, L. Q.; Tang, C.; Cui, X. Y.; Zheng, Y.; Wang, X. S.; Xu, H. L.; Zhang, S.; Shao, T.; Davey, K.; Qiao, S. Z. Efficient nitrogen fixation to ammonia through integration of plasma oxidation with electrocatalytic reduction. *Angew. Chem., Int. Ed.* **2021**, *133*, 14250–14256.

[20] Meng, Z.; Yao, J. X.; Sun, C. N.; Kang, X.; Gao, R.; Li, H. R.; Bi, B.; Zhu, Y. F.; Yan, J. M.; Jiang, Q. Efficient ammonia production beginning from enhanced air activation. *Adv. Energy Mater.* **2022**, *12*, 2202105.

[21] Ren, Y. W.; Yu, C.; Wang, L. S.; Tan, X. Y.; Wang, Z.; Wei, Q. B.; Zhang, Y. F.; Qiu, J. S. Microscopic-level insights into the mechanism of enhanced NH_3 synthesis in plasma-enabled cascade N_2 oxidation-electroreduction system. *J. Am. Chem. Soc.* **2022**, *144*, 10193–10200.

[22] Chen, D. W.; Liu, J. N.; Shen, J. J.; Zhang, Y. Q.; Shao, H. Y.; Chen, C.; Wang, S. Y. Electrocatalytic C–N couplings at cathode and anode. *Adv. Energy Mater.* **2024**, *14*, 2303820.

[23] Chen, K.; Zhang, Y.; Xiang, J. Q.; Zhao, X. L.; Li, X. G.; Chu, K. p-Block antimony single-atom catalysts for nitric oxide electroreduction to ammonia. *ACS Energy Lett.* **2023**, *8*, 1281–1288.

[24] Gao, C.; Low, J.; Long, R.; Kong, T. T.; Zhu, J. F.; Xiong, Y. J. Heterogeneous single-atom photocatalysts: Fundamentals and applications. *Chem. Rev.* **2020**, *120*, 12175–12216.

[25] Kaiser, S. K.; Chen, Z. P.; Faust Akl, D.; Mitchell, S.; Pérez-Ramírez, J. Single-atom catalysts across the periodic table. *Chem. Rev.* **2020**, *120*, 11703–11809.

[26] Lang, R.; Du, X. R.; Huang, Y. K.; Jiang, X. Z.; Zhang, Q.; Guo, Y. L.; Liu, K. P.; Qiao, B. T.; Wang, A. Q.; Zhang, T. Single-atom catalysts based on the metal-oxide interaction. *Chem. Rev.* **2020**, *120*, 11986–12043.

[27] Wang, Y.; Mao, J.; Meng, X. G.; Yu, L.; Deng, D. H.; Bao, X. H. Catalysis with two-dimensional materials confining single atoms: Concept, design, and applications. *Chem. Rev.* **2019**, *119*, 1806–1854.

[28] Cheng, Y. J.; Wang, H.; Song, H. Q.; Zhang, K.; Waterhouse, G. I. N.;

Chang, J. W.; Tang, Z. Y.; Lu, S. Y. Design strategies towards transition metal single atom catalysts for the oxygen reduction reaction—A review. *Nano Res. Energy* **2023**, *2*, e9120082.
[29] Wu, D. H.; Chen, K.; Lv, P.; Ma, Z. Y.; Chu, K.; Ma, D. W. Direct eight-electron N_2O electroreduction to NH_3 enabled by an Fe double-atom catalyst. *Nano Lett.* **2024**, *24*, 8502–8509.
[30] Shen, J.; Wang, D. S. How to select heterogeneous CO_2 reduction electrocatalyst. *Nano Res. Energy* **2024**, *3*, e9120096.
[31] Yan, J. X.; Ye, F. H.; Dai, Q. B.; Ma, X. Y.; Fang, Z. H.; Dai, L. M.; Hu, C. G. Recent progress in carbon-based electrochemical catalysts: From structure design to potential applications. *Nano Res. Energy* **2023**, *2*, e9120047.
[32] Zhai, J. W.; Dong, T. S.; Zhou, Y. M.; Min, J. J.; Yan, Y. L.; Garoufalis, C. S.; Baskoutas, S.; Xu, D. D.; Zeng, Z. P. Efficient band-edge emission from indirect bandgap semiconductor quantum dots upon shell engineering. *Nano Lett.* **2023**, *23*, 3239–3244.
[33] Min, J. J.; Zhai, J. W.; Dong, T. S.; Xu, D. D.; Yan, Y. L.; Garoufalis, C. S.; Baskoutas, S.; Zeng, Z. P.; Jia, Y. Design principle for tetrahedral semiconductors and their functional derivatives: Cation stabilizing charged cluster network. *Nano Lett.* **2023**, *23*, 4648–4653.
[34] Chen, K.; Zhang, G. K.; Li, X. T.; Zhao, X. L.; Chu, K. Electrochemical NO reduction to NH_3 on Cu single atom catalyst. *Nano Res.* **2023**, *16*, 5857–5863.
[35] Gou, W. K.; Sun, H. M.; Cheng, F. Y. Dual active sites engineering of electrocatalysts for alkaline hydrogen evolution. *Nano Res. Energy* **2024**, *3*, e9120121.
[36] Chen, K.; Ma, D. Y.; Zhang, Y.; Wang, F. Z.; Yang, X.; Wang, X. M.; Zhang, H.; Liu, X. J.; Bao, R.; Chu, K. Urea electrosynthesis from nitrate and CO_2 on diatomic alloys. *Adv. Mater.* **2024**, *36*, 2402160.
[37] Geng, J.; Ji, S. H.; Jin, M.; Zhang, C.; Xu, M.; Wang, G. Z.; Liang, C. H.; Zhang, H. M. Ambient electrosynthesis of urea with nitrate and carbon dioxide over iron-based dual-sites. *Angew. Chem., Int. Ed.* **2023**, *62*, e202210958.
[38] Panchal, D.; Lu, Q. Y.; Sakaushi, K.; Zhang, X. H. Advanced cold plasma-assisted technology for green and sustainable ammonia synthesis. *Chem. Eng. J.* **2024**, *498*, 154920.
[39] Wang, Y.; Xia, S.; Cai, R.; Zhang, J. F.; Yu, C. P.; Cui, J. W.; Zhang, Y.; Wu, J. J.; Wu, Y. C. Dynamic reconstruction of two-dimensional defective Bi nanosheets for efficient electrocatalytic urea synthesis. *Angew. Chem., Int. Ed.* **2024**, *63*, e202318589.
[40] Meng, N. N.; Ma, X. M.; Wang, C. H.; Wang, Y. T.; Yang, R.; Shao, J.; Huang, Y. M.; Xu, Y.; Zhang, B.; Yu, Y. F. Oxide-derived core–shell Cu@Zn nanowires for urea electrosynthesis from carbon dioxide and nitrate in water. *ACS Nano* **2022**, *16*, 9095–9104.
[41] Gao, Y. H.; Wang, J. N.; Sun, M. L.; Jing, Y.; Chen, L. L.; Liang, Z. Q.; Yang, Y. J.; Zhang, C.; Yao, J. N.; Wang, X. Tandem catalysts enabling efficient C–N coupling toward the electrosynthesis of urea. *Angew. Chem.* **2024**, *136*, e202402215.
[42] Lv, C. D.; Zhong, L. X.; Liu, H. J.; Fang, Z. W.; Yan, C. S.; Chen, M. X.; Kong, Y.; Lee, C.; Liu, D. B.; Li, S. Z. et al. Selective electrocatalytic synthesis of urea with nitrate and carbon dioxide. *Nat. Sustain.* **2021**, *4*, 868–876.
[43] Luo, Y. T.; Xie, K.; Ou, P. F.; Lavallais, C.; Peng, T.; Chen, Z.; Zhang, Z. Y.; Wang, N.; Li, X. Y.; Grigioni, I. et al. Selective electrochemical synthesis of urea from nitrate and CO_2 via relay catalysis on hybrid catalysts. *Nat. Catal.* **2023**, *6*, 939–948.